Highly Stretchable Bilayer Lattice Structures That Elongate via In-Plane Deformation

Burebi Yiming, Lei Wu, Mingqi Zhang, Zilong Han, Pei Zhao, Tiefeng Li, Zheng Jia,* and Shaoxing Qu

Many emerging technologies such as wearable batteries and electronics require stretchable functional structures made from intrinsically less deformable materials. The stretch capability of most demonstrated stretchable structures often relies on either initially out-of-plane configurations or the out-of-plane deflection of planar patterns. Such nonplanar features may dramatically increase the surface roughness, cause poor adhesion and adverse effects on subsequent multilayer processing, thereby posing a great challenge for flexible devices that require smooth surfaces (e.g., transparent electrodes in which flat-surface-enabled high optical transmittance is preferred). Inspired by the lamellar layouts of collagenous tissues, this work demonstrates a planar bilayer lattice structure, which can elongate substantially via only in-plane motion and thus maintain a smooth surfaces. The constructed bilayer lattice exhibits a large stretchability up to 360%, far beyond the inherent deformability of the brittle constituent material and comparable to that of state-of-the-art stretchable structures for flexible electronics. A stretchable conductor employing the bilayer lattice designs can remain electrically conductive at a strain of 300%, demonstrating the functionality and potential applications of the bilayer lattice structure. This design opens a new avenue for the development of stretchable structures that demand smooth surfaces.

1. Introduction

The quest for engineering structures that are ultrastretchable is ubiquitous, especially for the emerging field of wearable electronics and batteries that desire large deformability beyond 100% of strain.[1–3] Structural designs and the constituent materials are the two key factors in determining the stretchability. Unfortunately, most engineering materials including silicon, metal, ceramics, and plastics are intrinsically stiff and do not deform readily. Therefore, towards developing stretchable structures with the above materials that are much less stretchable, one needs to build strain releasing mechanisms into the structural designs via the manufacturing process.

The prevailing design paradigms can be categorized into four types. The first one relies on introducing serpentine-shaped patterns to otherwise unstretchable structures.[4–7] These designed structures are initially planar and consist of serpentine patterns in their plane. When being stretched, the structures made of serpentine patterns can deflect and twist out of the plane, aligning to the direction of the applied loading largely by rigid-body rotation, giving rise to substantially enhanced stretch capability. The resulting stress in the device structure is minimal. The second approach involves the fabrication of 3D architectures with out-of-plane features (e.g., waviness, coil, etc.) directly on elastomeric substrates.[8–11] Such structures accommodate large tensile deformation by flattening so that a large elongation only induces small strains in the structure. Third, structures with hollow-out, such as 2D nanomeshes and 3D microporous foams,[12–14] have been fabricated to achieve enhanced deformability. In such systems, the applied strains are accommodated largely by the rotation of the wall ligaments of the hollowed structures. Inspiration for the last design scheme comes from the arts of paper folding and cutting, i.e., the origami and kirigami. The designed deformable devices are usually formed by folding or cutting planar structures along predefined paths, and thus contain a series of rigid units connected through hinges.[15–20] When under tension, the structures unfold or elongate via the rotation of rigid units about the prescribed hinges, with each individual units remaining almost stress-free. Although the existing strategies have made tremendous progress, the fabrication techniques usually require multistep (e.g., wavy structure), costly, or material-specific (e.g., metal nanomesh) synthesis processes and thus are hardly applicable to other brittle materials. Moreover, the stretchability of stretchable structures designed by the above methods hinges upon the initial out-of-plane configurations (e.g., wavy structure, coils, and origami) or the out-of-plane deflection of initial flat patterns (e.g., serpentine,

B. Yiming, L. Wu, M. Zhang, Z. Han, Prof. P. Zhao,
Prof. T. Li, Prof. Z. Jia, Prof. S. Qu
Key Laboratory of Soft Machines and Smart Devices
of Zhejiang Province
Center for X-Mechanics
Department of Engineering Mechanics
Zhejiang University
Hangzhou 310027, China
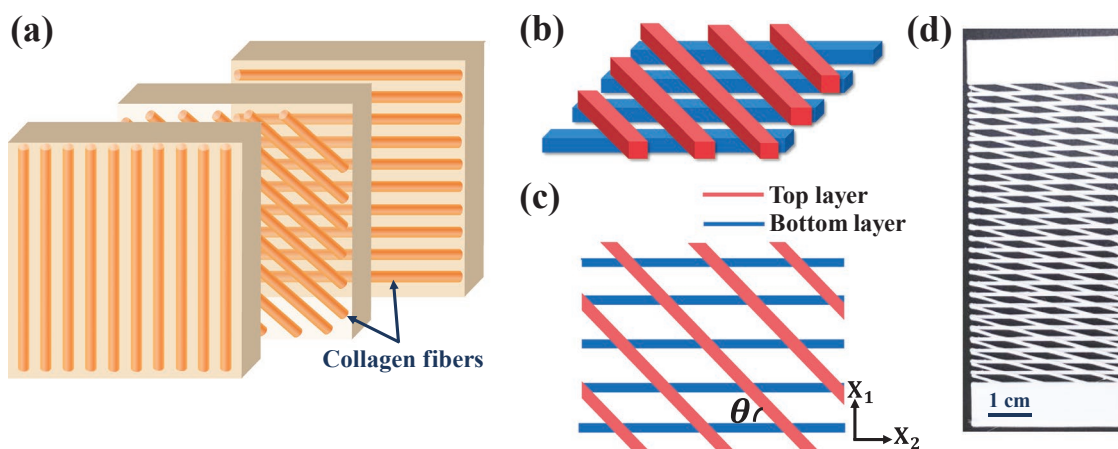E-mail: zheng.jia@zju.edu.cn

Figure 1. The design of the double-layer lattice structure. a) The lamellar structure of collagenous tissues such as osteons. Each individual lamella is composed of collagen fibers arranged in a preferred orientation. b) Schematic of the double-layer lattice structure. The fibers in the top and bottom layers are bonded to each other during the printing process. c) The top view of the double-layer lattice with the fibers in the top layer (red) making an angle θ to fibers in the bottom layer (blue). The horizontal and vertical arrows indicate the X_1 direction and X_2 direction, respectively. d) An exemplary printed lattice structure of $\theta = 15°$. (Scale bar 10 mm)

nanomesh, and kirigami). Integration of such stretchable structures into electronic devices usually relies on intricate device designs (such as patterned substrate) with prereserved spaces to accommodate the out-of-plane features, increasing the complexity of the fabrication process.[4] More importantly, surfaces with these out-of-plane features are uneven and non-smooth, which gives rise to high surface roughness,[21] poor adhesion,[22] and low optical transmittance.[23]

The advent of modern additive manufacturing techniques such as 3D printing offers rapid prototyping and demonstrate potent capability in printing a broad range of materials into complex structures, thereby opening new opportunities to manufacture novel engineering structures.[24–29] Aided with the 3D printing methods, engineers have recently constructed diverse wearable batteries and flexible electronic devices in a fast and scalable manner.[25,30–33] These efforts on imparting stretchability to electronic devices and batteries via 3D printing, however, rely on either inherently soft materials such as shape memory polymers and elastomers,[25,34] or brittle materials in the form of serpentine which usually requires out-of-plane space to accommodate the elongation and thus sacrifices flat and smooth surfaces.[35–37] To simultaneously attain smoothness and enhanced stretchability for stretchable structures with brittle constituting materials, new structure designs which can elongate significantly via in-plane motion is highly desirable, especially for flexible electronic devices that require flat and smooth surfaces such as transparent electrodes.[23] Notably, previous studies show that some serpentine and fractal structures can be designed to allow for large stretchability with only in-plane bending, the cross-sections have to be sufficiently thick to suppress the out-of-plane deflection. For instance, when subjected to tension, bioinspired composites with thick serpentine microstructures expand in the plane, with the out-of-plane deformation strongly suppressed.[38,39] Likewise, for thick fractal horseshoe constructs and thick self-similar serpentine of which the thickness is larger than the width, the deformation is governed by in-plane bending, instead of the out-of-plane buckling.[40–42] These designs need to be thick to suppress the

out-of-plane deflection. To this end, novel structural designs that lead to stretchability and flat surfaces are desired.

Here we present a general strategy and a simple method to digital fabrication of lattice structures via 3D printing that are highly stretchable and elongate without out-of-plane deflection. The natural inspiration of the structure design comes from flexible biological tissues, such as connective tissues, featuring a lamellar structure (**Figure 1**a). Each individual lamella is comprised of collagen fibers arranged in directional patterns,[43] with collagen fibrillar sliding acting as the prime deformation mechanism. To mimic the unique lamellar structure of collagen fibers in biological tissues, we print a bilayer lattice structure with each layer made of parallel fibers with a preferred orientation (Figure 1b; Figure S1, Supporting Information). The constructed double-layer structure exhibits a large stretchability of up to 360%, which is far beyond the intrinsic deformability of the brittle base material. Notably, the elongation of the lattice structure is accompanied by negligible out-of-plane deformation, retaining the flatness of the surface. The excellent stretch capability stems from the in-plane rotation of the fiber ligaments, largely in rigid-body motion, which accommodates the applied stretch without generating large strains in the base material. This enhancement mechanism is verified by finite element modeling (FEM). A stretchable conductor employing such bilayer lattice designs can remain electrically conductive at 300% strain, while exhibiting modest changes in electrical resistance. The application of the highly stretchable bilayer structure can be extended to other devices and systems such as flexible batteries, electrodes, and capacitors. Our work presents a simple yet effective strategy toward designing stretchable structures that elongate in plane, which is of great significance for structures and devices that require flat surfaces.

2. Results and Discussion

It is conceivable that the double-layer lattice structure can be constructed via various approaches. This paper adopts

extrusion-based additive manufacturing because of its simplicity and versatility, specifically using rigid but brittle polylactic acid (PLA) as the base material for demonstration herein. The printed lattice structure has final dimensions of 75 mm (l) × 35 mm (w) × 1 mm (t) and contains two layers (Figure 1b; Figure S1b, Supporting Information), each about 0.5 mm thick, that are bonded together at the fiber-fiber junctions during printing to form a "bilayer." The bottom layer has all fibers arranged in the horizontal direction (schematically illustrated as blue lines in Figure 1c). The top layer is composed of fibers oriented in a slanted direction (represented by red lines in Figure 1c). The structure of the bilayer lattice is thus characterized by the angle θ between the fibers in the top layer and those in the bottom layer. To investigate the role of the fiber arrangement in determining the stretchability of the bilayer lattice structure. Six sets of angle θ are considered, including $\theta = 15°, 20°, 30°, 45°, 60°,$ and $75°$. A photo of a printed sample of $\theta = 15°$ is shown in Figure 1d. More photo images of exemplary lattice structures can be found in Figure S1 in the Supporting Information.

2.1. Mechanical Tests of the Bilayer Lattice Structures

We prepared bilayer lattice structures with various angles θ and measured the mechanical properties of the bilayer structure in the X_1 direction (as illustrated in Figure 1c), which is perpendicular to the fibers in the bottom layer. It is found that the mechanical properties of the printed bilayer lattice structures are strongly dependent on the value of θ. **Figure 2**a compares the stretchability (aka, the ultimate tensile strain beyond which

the bilayer lattice structure ruptures) of samples with different θ. When the angle is decreased, the stretchability of the lattice structure increases, from ≈18% for $\theta = 75°$ to ≈360% for $\theta = 15°$ (Table S1, Supporting Information). The specimen of $\theta = 15°$ achieves a high stretchability of 360%, which is approximately 35 times that of PLA, the base material of the structure, and also higher than that of some typical stretchable interconnects for flexible electronics, such as serpentine (321%),[5] nanomesh (160%),[12] and wavy structures (130%),[10] and close to that of the kirigami sheet (370%).[20] Notably, it is conceivable that the stretchability of the lattice structure could be further enhanced by reducing the angle below 15°. This work, however, focuses on understanding the unique deformation mechanism of the double-layer lattice rather than attaining a record high ultimate tensile strain, such that the smallest angle we utilized in this study is 15°, which gives rise to a sufficiently large stretchability to meet the requirement of stretchable electronics and flexible batteries. The double-layer lattices presented here exhibit programmable Young's modulus (Figure 2b; Table S1, Supporting Information). As the angle is increased from 15° to 75°, The Young's modulus of double-layer lattice corresponding to $\theta = 15°, 45°,$ and $75°$ are 200 kPa, 14 MPa, and 128 MPa, respectively. To place these values in context, note the cartilage has elastic moduli ranging from 100 kPa to 2 MPa, the skin possesses stiffness of 8–40 MPa, and the tensile elastic moduli of ligament are between 80 and 700 MPa.[44] That is, the bilayer lattice structures with small angle (e.g., $\theta = 15°$ and 20°) exhibit similar stiffness to that of cartilage; while the bilayer lattices featuring modest ($\theta = 45°$) and large angles ($\theta = 75°$) resemble skins and ligaments in terms of the stiffness. Tough hydrogels are widely recognized as promising materials for
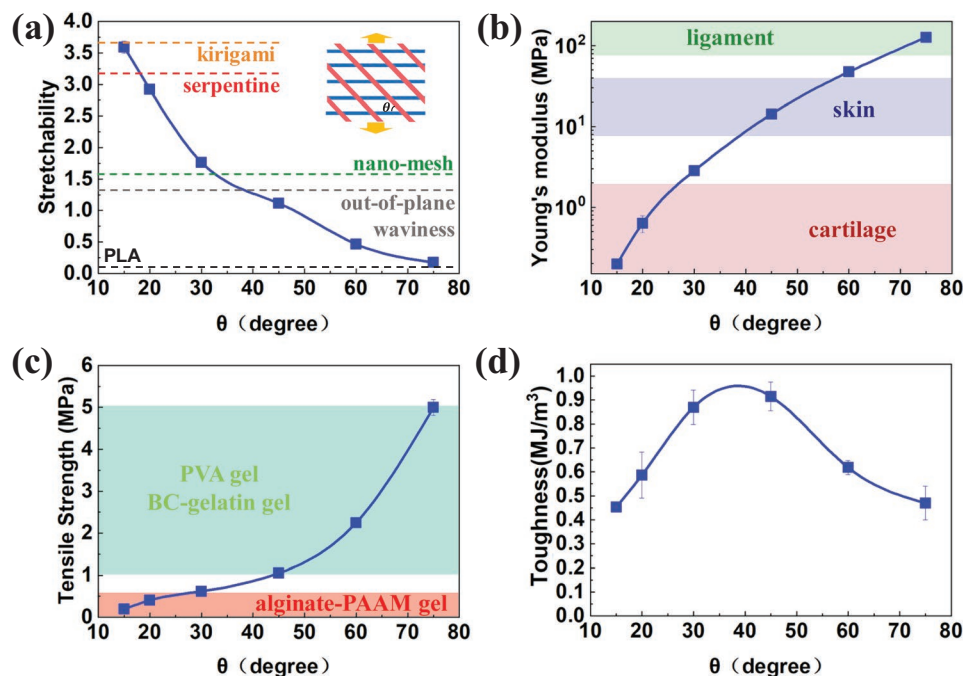

Figure 2. Mechanical properties of the bilayer lattice structures in the X_1 direction. a) The stretchability of the bilayer lattice structure, compared with other stretchable structures such as serpentine,[5] nanomesh,[12] and wavy structures,[10] and kirigami sheet.[20] The inset is a schematic showing the stretching along the X_1 direction. b) The Young's modulus of the bilayer structure. The structure exhibits highly tunable Young's modulus. c) The tensile strength. d) The toughness. Five samples are tested for each data point. Error bars represent standard deviation.

**ADVANCED
SCIENCE NEWS**
www.advancedsciencenews.com

**ADVANCED
FUNCTIONAL
MATERIALS**
www.afm-journal.de

artificial tissues, but they are rather compliant with low elastic moduli on the order of 10 kPa, below that of the abovementioned biological tissues. Thus, the double-layer lattice structures with proper angle can be applied to reinforce tough gels and engineer their stiffness, reducing the mechanical dissimilarities between natural tissues and man-made substitutes. The tensile strength of the bilayer lattices is comparable to hydrogels such as PVA gels and tough alginate-PAAM gels. The angle θ also plays a vital role in affecting the strength: the larger the angle, the higher the tensile strength of the double-layer lattice structure (Figure 2c). The toughness does not vary monotonically with θ but reached a maximum value at about $\theta = 45°$ (Figure 2d). The mechanical behavior of bilayer lattice structures is highly anisotropic because of the directional fiber arrangement. We also measured mechanical properties in the X_2 direction (Figure S2, Supporting Information). The stretch capability is rather inferior to that in the X_1 direction (Figure S2a, Supporting Information), and the measured Young's modulus is stiffer but much less tunable (Figure S2b, Supporting Information). The highly anisotropic stretch capability of the bilayer lattice might not be able to meet the requirement of practical applications in which biaxial stretchability is often required. Recent studies show that island-bridge architectures and hierarchical lattice designs constructed with serpentine microstructures can endow stretchable structures with isotropic in-plane stretchability. For example, bioinspired networks with horseshoe microstructures arranged in geometrical patterns can provide large isotropic in-plane deformability.[45–47] Moreover, electronic devices adopting the island-bridge architectures also yield excellent biaxial stretchability.[5] The bilayer lattice in the present study can be integrated into the island-bridge design as interconnects to construct biaxially stretchable devices (Figure S3, Supporting Information).

2.2. Deformation Mechanism of the Stretchable Bilayer Lattices

The stress–strain curves of bilayer lattices stretched in the X_1 direction are shown (**Figure 3**a,b; Figure S4, Supporting Information). The stress–strain curve of the bilayer structures featuring a small angle of $\theta = 15°$ consists of three regimes, namely, the elastic regime (Figure 3a, the purple section), the long plateau regime characterized by a zigzag behavior with extraordinary extensibility (Figure 3a, the cyan section), and the hardening regime with a rapid increase in stress (Figure 3a, the yellow section). These three regimes together give rise to a remarkable stretchability of 360% as demonstrated in the previous section of the present study. Lattices specified by $\theta = 20°$ and $\theta = 30°$ exhibit the same three-stage deformation behavior (Figure 3a, inset) and thus possess high rupture strains of 292% and 176%, respectively. In contrast, samples with comparatively larger angles (e.g., $\theta = 45°$, $60°$, and $75°$) show markedly different tensile behaviors. In the sample of $\theta = 45°$, the initial elastic regime and the subsequent long plateau regime are followed by a softening stage (Figure 3b), instead of the stiffening behavior observed in lattices with small angles, with the resultant stress continually dropping until rupture at ≈110% strain. In the lattices characterized by $\theta = 60°$ and $75°$, the sawtooth-shaped plateau stage disappears so that the stress–strain

curves are comprised of only two stages: the elastic regime and the softening regime, thereby leading to limited extensibility (Figure 3b, inset). Stress–strain curves of bilayer lattices stretched in the X_2 direction feature low rupture strains about 4% and do not vary significantly as the angle θ changes (Figures S5 and S6, Supporting Information).

To understand the basic mechanism underpinning the stretchability of the bilayer lattice structure, we examine the morphology change of the bilayer lattices subjected to elongation. The bilayer lattice with $\theta = 15°$ is initially patterned with rhombic unit cells demarcated by the PLA ligaments (Figure 3c; Movie S1, Supporting Information). When the applied stretch is small, which is the elastic regime, the initial rhombus unit cells deform elastically and remain rhombic (Figure 3c-(i)). Within the yielding plateau regime, the ligaments start to rotate in the plane of the sample to align with the applied load, extending the length of the structure without significantly stretching the ligament itself, thereby resulting in considerable extensibility. In this stage, the initially rhombic unit cells sequentially open up and deform into hexagons (Figure 3c-(ii)), indicating that the applied stretch is largely conformed by the in-plane rigid body rotation of the ligaments. Finally, at elevated stretch, the alignment of ligaments transforms the hexagons to rectangular unit cells (Figure 3c-(iii)), further elongation causes stretching of the ligaments, which drastically increases the resulting stress, giving rise to the hardening response before rupture. The observed sequential opening of meshes is also captured by the finite element simulations (Figure S7, Supporting Information). The simulated deformed morphology of the bilayer lattice agrees very well with the experimental results (Figure S7f, Supporting Information). Failure eventually sets in at the applied strain of 360% due to the high stress in the significantly strained ligaments and fiber–fiber junctions (Movie S1, Supporting Information). Notably, the bilayer lattice with small angles (e.g., $\theta = 15°$) presented in the current study has the capability of conforming large elongation by in-plane ligament rotation, largely in rigid body motion which effectively reduces the strain in the structure and produces high extensibility. The lattices of comparatively large θ lack such an effective strain-reduction mechanism. Unlike the elongation of the bilayer lattice featuring a small angle (i.e., $\theta = 15°$, $20°$, and $30°$) which occurs from sequential mesh opening, the bilayer structure featuring $\theta = 45°$ (Figure 3d), however, undergoes the formation of a necking band within the yielding plateau regime and then collapses with ligaments highly densified in the direction perpendicular to the applied pulling. The huge strain localization in the necking band induces severe damage and thus the softening behavior recorded in Figure 3b, eventually rupturing the structure at a strain of ≈110% which is much lower than the stretchability of the lattice with $\theta = 15°$. With θ further increased to 75°, the bilayer lattice fractures in a brittle manner at a strain of only 4.5% (Figure S8, Supporting Information). It is worthwhile to emphasize that the elongation of the bilayer lattice of $\theta = 15°$ is accompanied by in-plane deformation of the structure (Figure 3c; Movie S1, Supporting Information), in lieu of the out-of-plane deflection observed in most stretchable structures reported previously.[5,19,48] The large stretchability enabled by in-plane deformation is crucial for devices requiring a flat surface.
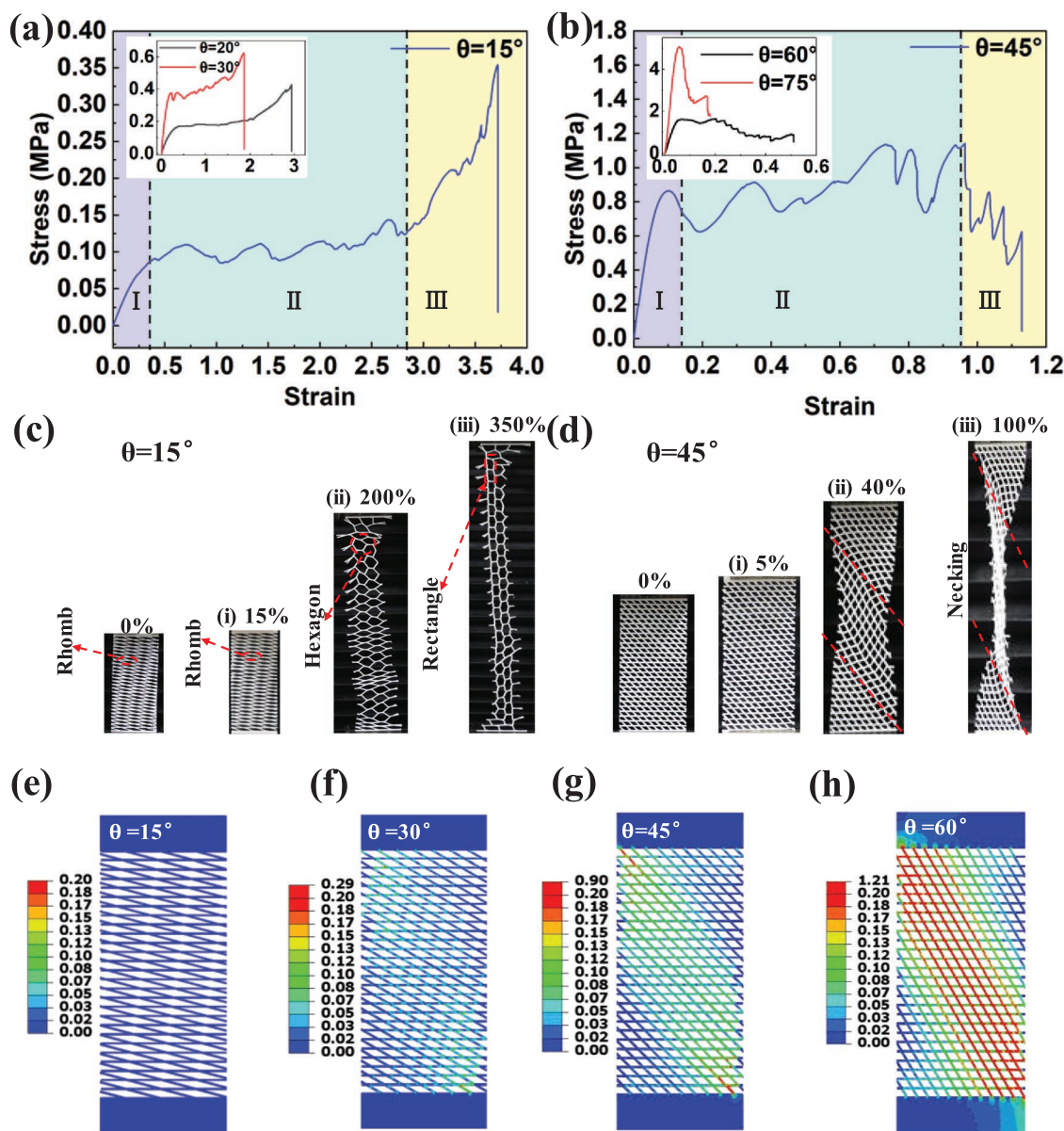
Figure 3. Deformation mechanism underpinning the stretchability of the bilayer lattice. a) Tensile stress–strain curves for bilayer lattice of $\theta = 15°$. Sections I (purple), II (cyan), and III (yellow) represent the regions of elastic deformation, yielding plateau regime, and hardening stage, respectively. Inset: Stress–strain curves for lattices with $\theta = 20°$ and $30°$. b) Tensile stress–strain curves for bilayer lattice of $\theta = 45°$. Herein, section III represents the regime of pattern collapse. Inset: Stress–strain curves for lattices with $\theta = 60°$ and $75°$. c) Snapshots showing that bilayer lattice of small angle ($\theta = 15°$) elongates via sequential mesh opening. d) Snapshots showing the necking band formation in bilayer lattice characterized by a relatively larger angle ($\theta = 45°$). The location and the orientation of the necking band are highlighted by the red dashed lines e–h) FEM results representing the strain distribution in the bilayer lattices that are subjected to an applied strain of 50%. Note that the results are shown in the undeformed configuration. The smaller the angle θ, the lower the resulting strain and the larger the extensibility. The bilayer lattice of $\theta = 15°$ features uniform strain distribution, while its counterpart of larger θ (= 45° or 60°) undergoes elevated strain in a localized slanted region, in agreement with the location and the orientation of the necking band.

To confirm the above-envisioned mechanistic understanding, we carried out FEM to simulate the development of strains in the bilayer lattice during stretching. The key trend revealed by the FEM results is that the strain experienced by the PLA fibers reduces drastically as the angle θ decreases (Figure 3e–h; Figure S9, Supporting Information). For example, under an applied tensile strain of 50%, the bilayer structure of $\theta = 60°$ undergoes strain up to 24% (Figure S9d and Table S2, Supporting Information), on the same order of the applied stretch. In sharp contrast, the bilayer lattice with $\theta = 15°$ under the relative elongation of 50% undergoes strains below 0.5%, less than one percent of the applied strain (Figure S9a and Table S2, Supporting Information), demonstrating the superb capability of releasing mechanical strain. That is, the bilayer lattice of
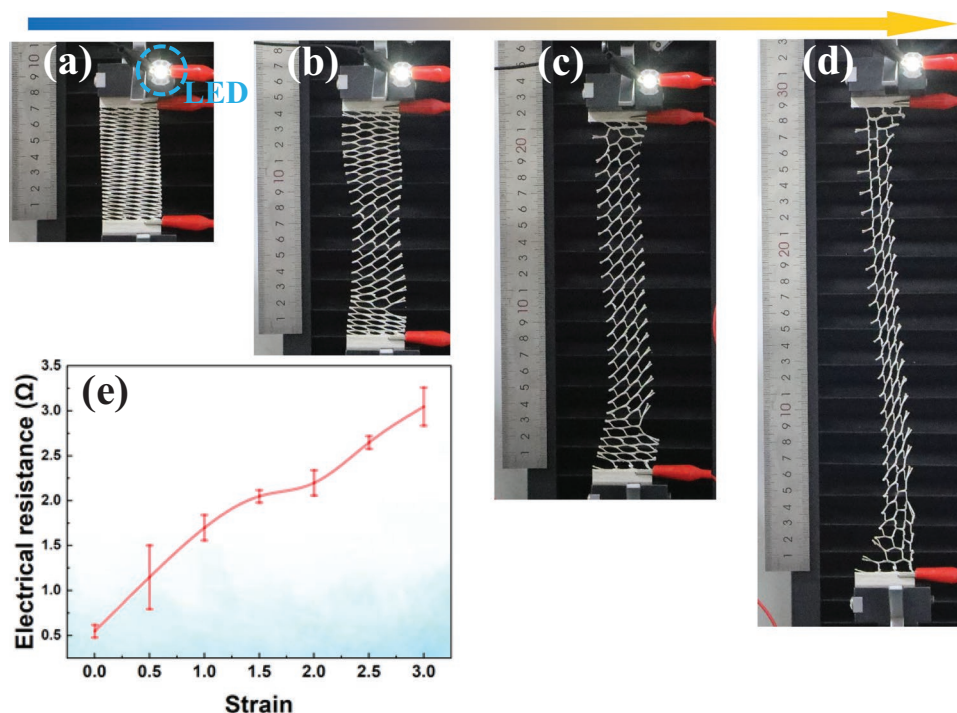
**ADVANCED
SCIENCE NEWS**
www.advancedsciencenews.com

**ADVANCED
FUNCTIONAL
MATERIALS**
www.afm-journal.de

Figure 4. Demonstration of the functionality of the bilayer lattice structure. a–d) Photographic images of the stretchable conductor constructed by coating silver paint on the bilayer lattice structure. The LED bulb remained illuminated for various levels of strain: 0% (virgin sample) (a), 100% (b), 200% (c), and 300% (d). The arrow indicates increasing strain level. e) The resistance of the conductor with different stretching strains.

$\theta = 15°$ elongates by the in-plane rigid-body rotation of ligaments and the resulting sequential opening of meshes so that a large elongation induces only small strains. Consequently, the bilayer lattice featuring smaller angle θ exhibits higher stretch capability. In addition to the difference in the magnitude of strain, the strain distribution in bilayer lattices of small angles contrasts with the strain profiles in structures featuring large angles. The strain is distributed uniformly in the bilayer lattice when the angle is small, i.e., $\theta = 15°$ (Figure 3e) and 30° (Figure 3f), while a localized slanted band of high strain are found in structures with large angles of $\theta = 45°$ (Figure 3g) and 60° (Figure 3h). The key observations in our experiments are replicated by the FEM results: The uniformity of strain distribution for small angles is in line with the sequential mesh opening revealed by Figure 3c, which allows for strain delocalization and thus enables exceptional extensibility. We note the FEM also accurately captures the region of localized high strain in the bilayer lattice with large θ, in good agreement with the location where the necking region takes place (Figure 3d). The emergence of the high-strain band causes necking and fracture of the samples at relatively small strains, as compared to their counterparts with small angles. To this end, high stretchability can be attained by imparting strain-releasing mechanism in the bilayer lattice: Enabled by the bilayer lattice design of small θ, the fibers rotate in-plane via rigid body motion so that the meshes can open up fully and sequentially to extend the structure with large elongation but small mechanical strain.

2.3. Applications of the Bilayer Lattice Structures

To highlight the potential application of the bilayer lattice structure, we constructed a stretchable conductor, aka a bilayer-lattice conductive interconnect, by coating a thin layer of silver paint on the surface of the bilayer lattice. To visually illustrate the conductivity of the conductor subjected to stretch, photo images of the bilayer-lattice interconnect being used to power a light-emitting diode (LED) bulb are shown in **Figure** 4a–d. The LED remained lit with illumination as the bilayer-lattice interconnect was stretched to a strain of 300%. During the stretching, the silver layer demonstrates good adhesion with the double-lattice structure and no cracks were found in the silver coating. Figure 4e shows the resistance of the bilayer lattice interconnect exhibits a sixfold increase when being elongated to a strain of 300%, which is mainly due to the elongation and thinning of the silver coating rather than the fracture of the coating. It is reasonable to expect that the stretchable conductor based on the bilayer-lattice design can impart conductivity and stretchability in stretchable devices, without increasing the surface roughness by out-of-plane deflection.

2.4. Comparison between the Bilayer Lattice and the Single-Layer Lattice

As noted at the beginning of this paper, the natural inspiration for the bilayer lattice design comes from the layered
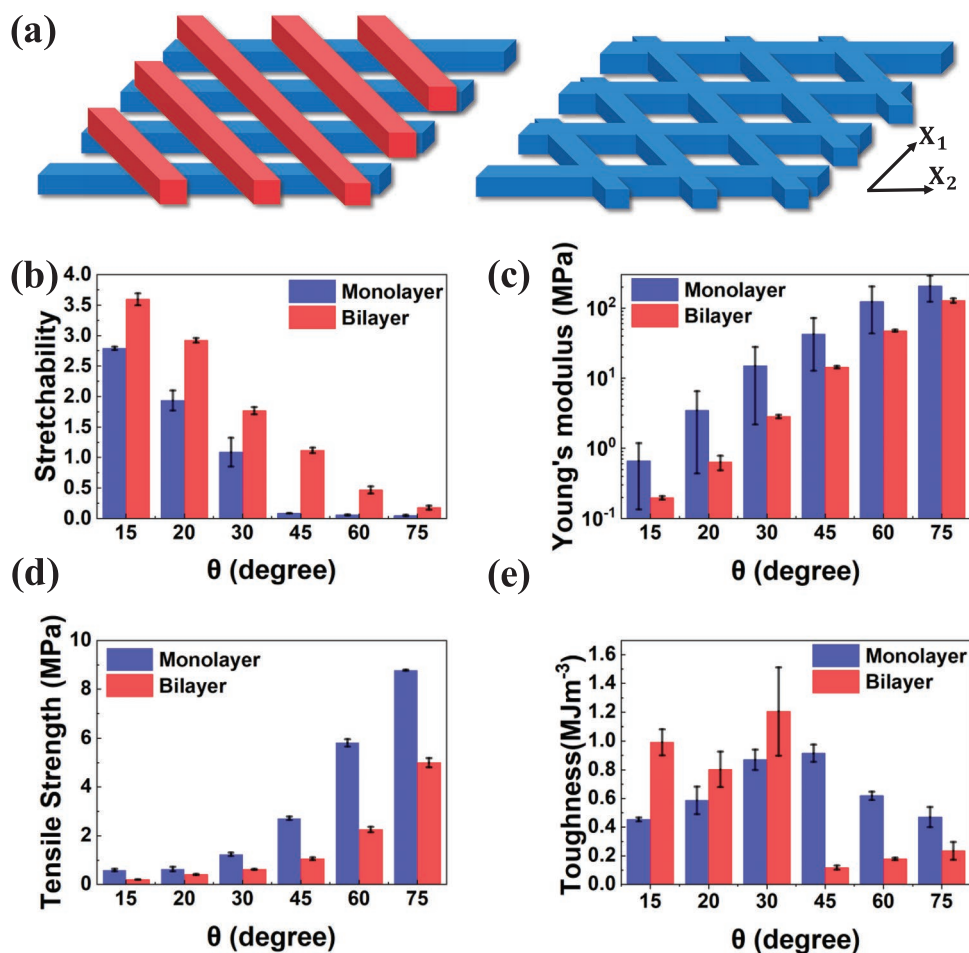
Figure 5. Comparison of the mechanical properties of bilayer lattices with monolayer networks. a) Schematic of bilayer lattices and monolayer networks. The first and second layers are highlighted by blue and red, respectively. The arrows indicate the stretching directions. b) Compared with single-layer networks, the bilayer lattices have improved stretchability in the X_1 direction. c) The Young's moduli of bilayer lattices are lower than that of the monolayer network, indicating that the bilayer lattices are more compliant. d) The bilayer lattices have lower strength. e) Comparison of the toughness of the bilayer and monolayer structures. Error bars represent the standard deviation.

arrangement of collagen fibers in cartilages or osteons. To gain more insights into the stretchability of the structure, we further compared the mechanical properties of the double-layer lattice in the X_1 direction (**Figure 5**a, left panel) to its single-layer counterpart (Figure 5a, right panel). The left and right panels of Figure 5a show a schematic of the perspective view of the bilayer lattice and the monolayer lattice, respectively. The printed monolayer lattice contains PLA fibers of two different orientations arranged in the same layer, forming a single-layer network (Figure S1c,d, Supporting Information). As compared to the bilayer lattices, the monolayer ones are also characterized by the angle θ and contain fibers of the same size. Results in Figure 5b indicate that the bilayer designs have improved stretchability in the X_1 direction, compared with the monolayer networks. The stretchability of the bilayer lattice of $\theta = 15°$ exceeds that of its single-layer counterpart by 80% (Figure 5b; Table S1, Supporting Information). The difference in the stretchability is more significant for large angles. The rupture strain of bilayer lattices of $\theta = 45°$, 60°, and 75° is about 13 times, 8 times, and 3 times higher than that of their

single-layer counterparts, respectively, showing the effectiveness of the bilayer configuration in enabling effective strain releasing and exceptional stretchability. The disparity between the stretch capability of the bilayer lattice and that of the monolayer network can be understood as follows. In the single-layer network, fibers of different orientations cross and merge at the fiber–fiber junctions. In the language of mechanics, the fiber–fiber junction poses a fixed-end boundary condition to the PLA ligaments that strongly restricts their in-plane rotation, thereby hindering the strain releasing which largely relies on the rigid-body rotation of ligaments. The flexibility of the network is thus compromised. For example, the fracture of the single-layer network featuring $\theta = 45°$ is rather brittle (Figure S10, Supporting Information), with a rupture strain of only 4.9%, comparable to that of the base material, the PLA. By contrast, bilayer lattices are formed by welding the two layers via interfacial joints where the bottom surface of the top layer is bonded to the top surface of the bottom layer. Compared to the fiber–fiber junctions in the monolayer network, the interfacial joints only impose modest mechanical constraints, such that ligaments

in both layers rotate readily in their plane to accommodate the elongation of the lattice. Consequently, the double-layer lattices are more flexible and compliant in response to the applied elongation compared to single-layer networks, thereby producing an elevated rupture strain (Figure 5b) but smaller Young's modulus (Figure 5c) and tensile strength (Figure 5d). The toughness of bilayer lattices of small angles (e.g., $\theta = 15°$, $20°$, and $30°$) is larger than that of the corresponding monolayer designs (Figure 5d), owing to the superior stretchability of the bilayer structures.

3. Conclusion

In summary, inspired by the lamellar structure of collagen tissues such as cartilages and osteons, we have presented a bilayer lattice structural design with superb stretch capability that can elongate substantially via only in-plane deformation, which is fundamentally different from most stretchable structures in flexible electronics relying on the out-of-plane deflection. Such a feature is highly desirable for devices that require flat surfaces and low surface roughness, such as flexible transparent electrodes. We have demonstrated this design with PLA (an inherently brittle material with rupture strain about 10%) and 3D-printing technique that lead to an exceptional stretchability up to 360%, about 35 times that of the base material, and also higher than that of some typical stretchable structures for flexible electronics with rupture strain ranging from 100% to 300%.[5,10,12] Mechanical properties such as Young's modulus of the bilayer lattices can be programmed by tuning the angle θ, to match that of various biological tissues. This general and simple structural design can be readily adapted to many other brittle materials to endow them with exceptional stretch capability. The key deformation mechanism underpinning the large stretchability is the sequential opening of meshes by in-plane rotation of fiber ligaments, largely in rigid-body motion that accommodates applied elongation while effectively reducing the material strain. The above-envisioned strain-releasing mechanism has been verified by the results of finite element simulation. We further revealed that the counterintuitive bilayer design is superior to its more common monolayer counterpart in terms of extensibility and compliance. To demonstrate potential applications, we produced an example stretchable conductor by coating silver paint on the stretchable bilayer lattices, which remains electronically conductive at 300% strain. It is expected that the bilayer lattices will enable novel designs of electronic devices such as flexible batteries, electrodes, and capacitors, with the hope of simultaneously attaining stretchability and smooth surfaces.

4. Experimental Section

Printing: Digital fabrication was done using a commercial 3D printer MakerBot Replicator + (MakerBot, USA). Polyactic acid (MakerBot, USA) is the base material used. All samples were produced at room temperature while the nozzle temperature was controlled at 230 °C. The printing speed was set to be 150 mm s^{-1} and the thickness of each PLA filament extruded through the nozzle was fixed at 100 μm. For the bilayer lattices, each lamella consists of five layers of filaments and

exhibits a rectangular-shaped cross-section with a width of $W = 600$ μm and a thickness of 500 μm. The spacing between adjacent fibers is set to be 2 mm to ensure high printing quality. For the single-layer structures, each individual fiber has a rectangular-shaped cross-section with the same width and thickness as the fiber of double-layer lattices.

Mechanical Testing: The tensile testing was conducted using a tensile machine (Suns UTM2503) with a 50 N load cell and a 500 N load cell. All tests were performed taking 1200 data points per minute. A displacement rate of 5 mm min^{-1} was employed to apply a strain rate of 0.1% s^{-1}. At least five samples were tested for each data point reported in Figures 2, 4, and 5.

Finite Element Modeling: The strain development of the bilayer lattice under tension was computationally studied by the commercial finite element package ABAQUS 2018. The simulated models were generated by the CAD design code SOLIDWORKS 2018. An elastic constitutive law with Young's modulus of 1 GPa and Poisson's ratio of 0.3 was used for PLA. The bilayer lattice structures were meshed with 4-node tetrahedron element (C3D4). The Nlgeom setting needs to be turned on to take into account the large rotation of ligaments during stretching. All simulations have been conducted in a quasi-static manner.

Supporting Information

Supporting Information is available from the Wiley Online Library or from the author.

Conflict of Interest

The authors declare no conflict of interest.

Keywords

bilayer lattice structures, in-plane elongation, stretchability, stretchable conductors

[1] Y. J. Hong, H. Jeong, K. W. Cho, N. Lu, D.H. Kim, *Adv. Funct. Mater.* **2019**, *29*, 1808247.

[2] W. Liu, M. S. Song, B. Kong, Y. Cui, *Adv. Mater.* **2017**, *29*, 1603436.

[3] C. Wang, C. Wang, Z. Huang, S. Xu, *Adv. Mater.* **2018**, *30*, 1801368.

[4] Q. Zhao, Z. Liang, B. Lu, Y. Chen, Y. Ma, X. Feng, *Adv. Mater. Technol.* **2018**, *3*, 1800169.

[5] S. Xu, Y. Zhang, J. Cho, J. Lee, X. Huang, L. Jia, J. A. Fan, Y. Su, J. Su, H. Zhang, H. Cheng, B. Lu, C. Yu, C. Chuang, T. i. Kim, T. Song, K. Shigeta, S. Kang, C. Dagdeviren, I. Petrov, P. V. Braun, Y. Huang, U. Paik, J. A. Rogers, *Nat. Commun.* **2013**, *4*, 1543.

[6] D. H. Kim, N. Lu, R. Ma, Y. S. Kim, R. H. Kim, S. Wang, J. Wu, S. M. Won, H. Tao, A. Islam, K. J. Yu, T. i. Kim, R. Chowdhury, M. Ying, L. Xu, M. Li, H. J. Chung, H. Keum, M. McCormick, P. Liu,

**ADVANCED
SCIENCE NEWS**

www.advancedsciencenews.com

**ADVANCED
FUNCTIONAL
MATERIALS**

www.afm-journal.de

Y. W. Zhang, F. G. Omenetto, Y. Huang, T. Coleman, J. A. Rogers, *Science* **2011**, *333*, 838.

[7] K. Li, X. Cheng, F. Zhu, L. Li, Z. Xie, H. Luan, Z. Wang, Z. Ji, H. Wang, F. Liu, Y. Xue, C. Jiang, X. Feng, L. Li, J. A. Rogers, Y. Huang, Y. Zhang, *Adv. Funct. Mater.* **2019**, *29*, 1806630.

[8] D. Y. Khang, H. Q. Jiang, Y. Huang, J. A. Rogers, *Science* **2006**, *311*, 208.

[9] K. I. Jang, K. Li, H. U. Chung, S. Xu, H. N. Jung, Y. Yang, J. W. Kwak, H. H. Jung, J. Song, C. Yang, A. Wang, Z. Liu, J. Y. Lee, B. H. Kim, J. H. Kim, J. Lee, Y. Yu, B. J. Kim, H. Jang, K. J. Yu, J. Kim, J. W. Lee, J. W. Jeong, Y. M. Song, Y. Huang, Y. Zhang, J. A. Rogers, *Nat. Commun.* **2017**, *8*, 15894.

[10] D. Qi, Z. Liu, M. Yu, Y. Liu, Y. Tang, J. Lv, Y. Li, J. Wei, B. Liedberg, Z. Yu, X. Chen, *Adv. Mater.* **2015**, *27*, 3145.

[11] K. Liu, B. Kong, W. Liu, Y. Sun, M.-S. Song, J. Chen, Y. Liu, D. Lin, A. Pei, Y. Cui, *Joule* **2018**, *2*, 1857.

[12] S. Huang, Y. Liu, Y. Zhao, Z. Ren, C. F. Guo, *Adv. Funct. Mater.* **2019**, *29*, 1805924.

[13] Y. Wang, Q. Liu, J. Zhang, T. Hong, W. Sun, L. Tang, E. Arnold, Z. Suo, W. Hong, Z. Ren, C. F. Guo, *Adv. Mater.* **2019**, *31*, e1902955.

[14] H. Vandeparre, Q. Liu, I. R. Minev, Z. Suo, S. P. Lacour, *Adv. Mater.* **2013**, *25*, 3117.

[15] Z. Song, T. Ma, R. Tang, Q. Cheng, X. Wang, D. Krishnaraju, R. Panat, C. K. Chan, H. Yu, H. Jiang, *Nat. Commun.* **2014**, *5*, 3140.

[16] Z. Song, X. Wang, C. Lv, Y. An, M. Liang, T. Ma, D. He, Y. J. Zheng, S. Q. Huang, H. Yu, H. Jiang, *Sci. Rep.* **2015**, *5*, 10988.

[17] Y. Tang, G. Lin, L. Han, S. Qiu, S. Yang, J. Yin, *Adv. Mater.* **2015**, *27*, 7181.

[18] Y. Tang, G. Lin, S. Yang, Y. K. Yi, R. D. Kamien, J. Yin, *Adv. Mater.* **2017**, *29*, 1604262.

[19] T. C. Shyu, P. F. Damasceno, P. M. Dodd, A. Lamoureux, L. Xu, M. Shlian, M. Shtein, S. C. Glotzer, N. A. Kotov, *Nat. Mater.* **2015**, *14*, 785.

[20] Y. S. Guan, Z. Zhang, Y. Tang, J. Yin, S. Ren, *Adv. Mater.* **2018**, *30*, 1706390.

[21] M. Drack, I. Graz, T. Sekitani, T. Someya, M. Kaltenbrunner, S. Bauer, *Adv. Mater.* **2015**, *27*, 34.

[22] M. Yunusa, G. J. Amador, D.M. Drotlef, M. Sitti, *Nano Lett.* **2018**, *18*, 2498.

[23] Y. Fang, Z. Wu, J. Li, F. Jiang, K. Zhang, Y. Zhang, Y. Zhou, J. Zhou, B. Hu, *Adv. Funct. Mater.* **2018**, *28*, 1705409.

[24] Z. C. Eckel, C. Zhou, J. H. Martin, A. J. Jacobsen, W. B. Carter, T. A. Schaedler, *Science* **2016**, *351*, 58.

[25] A. D. Valentine, T. A. Busbee, J. W. Boley, J. R. Raney, A. Chortos, A. Kotikian, J. D. Berrigan, M. F. Durstock, J. A. Lewis, *Adv. Mater.* **2017**, *29*, 1703817.

[26] Z. Chen, D. Zhao, B. Liu, G. Nian, X. Li, J. Yin, S. Qu, W. Yang, *Adv. Funct. Mater.* **2019**, *29*, 1900971.

[27] D. Kokkinis, F. Bouville, A. R. Studart, *Adv. Mater.* **2018**, *30*, 1705808.

[28] Y. Kim, H. Yuk, R. Zhao, S. A. Chester, X. Zhao, *Nature* **2018**, *558*, 274.

[29] M. S. Pham, C. Liu, I. Todd, J. Lertthanasarn, *Nature* **2019**, *565*, 305.

[30] D. Cao, Y. Xing, K. Tantratian, X. Wang, Y. Ma, A. Mukhopadhyay, Z. Cheng, Q. Zhang, Y. Jiao, L. Chen, H. Zhu, *Adv. Mater.* **2019**, *31*, 1807313.

[31] H. Yang, W. R. Leow, X. Chen, *Small Methods* **2018**, *2*, 1700259.

[32] Y. Wang, C. Chen, H. Xie, T. Gao, Y. Yao, G. Pastel, X. Han, Y. Li, J. Zhao, K. Fu, L. Hu, *Adv. Funct. Mater.* **2017**, *27*, 1703140.

[33] M. A. Bessa, P. Glowacki, M. Houlder, *Adv. Mater.* **2019**, *31*, e1904845.

[34] T. Mu, L. Liu, X. Lan, Y. Liu, J. Leng, *Compos. Sci. Technol.* **2018**, *160*, 169.

[35] S. R. Shin, R. Farzad, A. Tamayol, V. Manoharan, P. Mostafalu, Y. S. Zhang, M. Akbari, S. M. Jung, D. Kim, M. Comotto, N. Annabi, F. E. Al-Hazmi, M. R. Dokmeci, A. Khademhosseini, *Adv. Mater.* **2016**, *28*, 3280.

[36] M. D. Dickey, *Adv. Mater.* **2017**, *29*, 1606425.

[37] H. Wei, K. Li, W. G. Liu, H. Meng, P. X. Zhang, C. Y. Yan, *Adv. Eng. Mater.* **2017**, *19*, 1700341.

[38] K.I. Jang, H. U. Chung, S. Xu, C. H. Lee, H. Luan, J. Jeong, H. Cheng, G.T. Kim, S. Y. Han, J. W. Lee, J. Kim, M. Cho, F. Miao, Y. Yang, H. N. Jung, M. Flavin, H. Liu, G. W. Kong, K. J. Yu, S. I. Rhee, J. Chung, B. Kim, J. W. Kwak, M. H. Yun, J. Y. Kim, Y. M. Song, U. Paik, Y. Zhang, Y. Huang, J. A. Rogers, *Nat. Commun.* **2015**, *6*, 6566.

[39] Z. Xue, H. Song, J. A. Rogers, Y. Zhang, Y. Huang, *Adv. Mater.* **2019**, https://doi.org/10.1002/adma.201902254.

[40] Y. Su, X. Ping, K. J. Yu, J. W. Lee, J. A. Fan, B. Wang, M. Li, R. Li, D. V. Harburg, Y. Huang, C. Yu, S. Mao, J. Shim, Q. Yang, P.Y. Lee, A. Armonas, K.J. Choi, Y. Yang, U. Paik, T. Chang, T. J. Dawidczyk, Y. Huang, S. Wang, J. A. Rogers, *Adv. Mater.* **2017**, *29*, 1604989.

[41] Y. Zhang, H. Fu, Y. Su, S. Xu, H. Cheng, J. A. Fan, K. C. Hwang, J. A. Rogers, Y. Huang, *Acta Mater.* **2013**, *61*, 7816.

[42] Q. Ma, Y. Zhang, *J. Appl. Mech.* **2016**, *83*, 111008.

[43] U. G. K. Wegst, H. Bai, E. Saiz, A. P. Tomsia, R. O. Ritchie, *Nat. Mater.* **2015**, *14*, 23.

[44] J. Li, Z. Suo, J. J. Vlassak, *J. Mater. Chem. B* **2014**, *2*, 6708.

[45] Y. Ma, X. Feng, J. A. Rogers, Y. Huang, Y. Zhang, *Lab Chip* **2017**, *17*, 1689.

[46] J. Liu, H. Song, Y. Zhang, *ACS Appl. Mater. Interfaces* **2019**, *11*, 36100.

[47] Q. Ma, H. Cheng, K. I. Jang, H. Luan, K. C. Hwang, J. A. Rogers, Y. Huang, Y. Zhang, *J. Mech. Phys. Solids* **2016**, *90*, 179.

[48] C. F. Guo, T. Sun, Q. Liu, Z. Suo, Z. Ren, *Nat. Commun.* **2014**, *5*, 3121.

1909473 (9 of 9)